

Computational Fluid Dynamics Simulation of Structured Packing

Scott A. Owens, Michael R. Perkins, and R. Bruce Eldridge*

Process Science and Technology Center, The University of Texas, Austin, Texas 78712, United States

Karl W. Schulz

Texas Advanced Computing Center, The University of Texas, Austin, Texas 78712, United States

Richard A. Ketcham

Jackson School of Geosciences, The University of Texas, Austin, Texas 78712, United States

ABSTRACT: An electronic representation of Sulzer's Mellapak N250Y structured packing was generated by subjecting a physical packing element to CT scan. The resulting file was imported into a three-dimensional imaging program and then copied, translated, and rotated to create a stack of three packing elements. This stack was then inserted into an open-ended cylindrical surface to approximate a packed column. The resulting three-dimensional image file was imported into the Star-CCM+ CFD software and meshed using the Surface Remesher and Polygonal Volume Meshing routines to create a high-quality volume mesh. The mesh was then utilized to produce a series of CFD simulations. Flow rates were chosen so that the velocities studied would match those commonly employed in the vapor phase of industrial distillation columns. The pressure drop across the packing was monitored during iterative computations, and its rate of change was used to judge convergence. The simulation predictions were shown to be in good agreement with experiments that measured pressure drop in an analogous geometry and flow range.

MOTIVATION

Distillation is the most common unit operation employed to achieve the necessary chemical separations in the refining and chemical industry. This fact is borne out by the over 40 000 distillation columns in the United States, which require more than 5.06×10^{18} J (4.8×10^{15} BTU) annually.¹ That translates to over 40% of the energy used in refining and chemical processing industries.¹

Because of the extensive use of distillation columns and their long lifespan, even modest improvements in design or operation will result in significant cost savings. Most distillation columns are heated by steam produced by fossil fuels. Reducing the consumption of these expensive fuels will yield immediate cost savings and will have the added benefit of limiting CO₂ emissions.

Optimization of distillation performance has long been constrained by a lack of comprehensive and robust models of fluid flow. The complexity of the two-phase flow field coupled with a dearth of methods to directly observe it have precluded a thorough understanding of the flow phenomena and the development of design and operation principles rooted in fluid flow theory. Current distillation design and operation models employ a handful of correlative relationships.^{2–4} The combination of high-performance computing clusters and computational fluid dynamics (CFD) simulation software is employed in the aerospace, automotive, and marine industries to enhance performance, decrease design costs, and accelerate the adoption of new designs. These tools promise similar improvements in distillation design and performance.

This work demonstrates a means by which complicated flow systems, specifically whole elements of structured packings, can

be quickly and accurately simulated. Previously, the complicated natures and large simulation volumes required to model structured packing have prevented this method of study. This method does not require simplifying assumptions, and the accuracy of the geometry can easily be numerically quantified and studied as an independent parameter on simulation accuracy. A high-fidelity computational geometry was generated by importing the results of an X-ray computed tomography (CT) scan of a common structured packing. Grid generation was performed automatically using adaptive mesh generation software with user-specified minimum and maximum grid spacings, as well as cell growth rate. Using this method, a high-fidelity, unstructured CFD mesh can be generated and ready for simulation in hours instead of weeks.

BACKGROUND

Literature Review. *CFD Studies of Packed Columns.* The earliest efforts at three-dimensional CFD simulation of structured packing sought to reduce the computational needs of simulation by modeling volume elements, or representative elementary units (REUs), of structured packing separately.^{5–10} Petre et al. modeled single-phase vapor flow through four representative volumes in three different packing designs at Reynolds numbers ranging from creeping to turbulent flow.⁵ Pressure losses for each REU were

Received: June 25, 2012

Revised: October 14, 2012

Accepted: January 7, 2013

Published: January 7, 2013

obtained directly from CFD simulation. Macroscale pressure drops were calculated by multiplying by the number of REUs in a given packing and using empirical interaction parameters. The CFD predictions proved to be more accurate than the models published by Brunnazi and Paglanti, Meier et al., Olujic, and Rocha et al.^{11–15}

The REU method was extended by Larachi et al. to simulate the single-phase pressure drop of both Montz B1-250.45 and the higher-capacity version, Montz B1-250.45+B1V.⁶ The simulations showed the energy efficiency of the vertical-channel REUs to be 30% higher than that of REUs that transitioned between 45° channels. However, this was a minor contribution to the macroscale pressure loss.

Ataki and Bart performed REU CFD simulations of the X shape found in Rombopak 4 M to determine the effect of liquid viscosity on the wetted area.⁷ FLUENT's Volume of Fluid (VOF) package was used to simulate the liquid flow and track the vapor–liquid interface. The CFD predictions were found to be more accurate over a wider range of fluid properties and flow rates than the Billet–Schultes, Shi–Mersmann, SRP, Delft, and Onda models.

Raynal et al. employed the VOF model to perform REU CFD simulations to study the irrigated pressure drop of three geometries.⁸ The first was a three-dimensional representation of two intersecting channels and was shown to overestimate the dry pressure drop. A second geometry consisting of the space between two sheets of packing 200 mm wide and 100 mm tall was used to calculate specific pressure drop. Pressure measurements were made at two heights in the interior (23 mm and 78.55 mm) of the packing. The third geometry was a two-dimensional cross section of the second geometry. When compared to gamma ray tomography experiments, the two-dimensional simulation was found to underpredict holdup by approximately 20%.

Szukzeqská et al. employed a two-dimensional CFD model to study liquid behavior under two-phase countercurrent flow between vertical flat and corrugated plates.⁹ Both the simulation and experiment failed to achieve total water coverage of either plate. The water formed streams in both cases. By contrast, toluene achieved complete wetting in both simulation and experiment. The simulation predicted that the effective area of toluene would surpass the area of the packing as a result of wave formation.

In 2007, Raynal and Royon-Lebeaud employed a multiscale approach that incorporated CFD to model gas–liquid flow through a column equipped with an approximation of the Mellapak 250Y structured packing.¹⁰ Limited small-scale simulations were employed to determine liquid holdup, interstitial velocities, and irrigated pressure drop. These results were used in CFD simulations that approximated the packing as a porous medium. The liquid holdup and pressure drop found previously were used to fine tune the properties of the porous medium.

Mahr and Mewes also approximated structured packing as a porous medium.^{16,17} With this approximation, a macroscopic column (0.288-m diameter × 0.84-m height, packed with four elements) can be modeled using the elementary cell model. The researchers introduced liquid feed from a point source immediately above the topmost packing and simulated the radial spreading throughout the packing elements. Experimental validation of the predicted spreading was accomplished through the use of X-ray radiography to monitor liquid distribution in a two-dimensional section of packing. The elementary cell model was found to accurately predict liquid spreading over macroscopic scales.

Jafari et al. studied flow through a randomly packed bed of hard spheres.¹⁸ A smooth cylinder geometry and a rough cylinder geometry were used with velocity inlet and pressure outlet conditions. The pressure drop calculations matched data from the literature quite well. Interestingly, they developed an expression for dispersivity to be used in conjunction with their CFD program. The results were used to calculate permeability and then compared to correlations (Kozeny–Carman equation). The maximum error for pressure drop was less than 10%. Porosity results were compared to the Kozeny–Carman correlation at porosities below 0.6. Calculated dispersivities were in close agreement with experimental results.

A coupled discrete-element method (DEM) and CFD approach was employed by Bai et al. to study pressure drop across packed-bed reactors with low ratios between the tube and particle diameters ($D/d < 4$).¹⁹ The DEM was used to create a simplified representation of spherical and cylindrical catalysts in a packed bed, and CFD was used to model flow through the bed. The individual particles were shrunk to 0.5–2% of their diameter after “packing” to avoid particle-to-particle contact, which complicates CFD meshing. This created a discrepancy between the modeled and actual void fraction observed with these particles. The authors remedied this discrepancy by multiplying the CFD-predicted pressure drop by a “pressure correction factor”. This allowed the results to be compared with experimental results taken from a laboratory-scale packed bed (~150 particles) and an industrial-scale packed bed (~1500 particles). The authors used the standard $k-\epsilon$ model, the realizable $k-\epsilon$ model, the renormalization group (RNG) $k-\epsilon$ model, the Spalart–Allmaras model, the standard and shear stress transport (SST) $k-\omega$ models, and the Reynolds stress model (RSM) to model the flow. All of the turbulence models used underpredicted the pressure drop both before and after correction for the void fraction. The Spalart–Allmaras model displayed the most error, and the RSM proved to be most accurate. Although the RSM model was the most accurate, the runtime for this model was nearly 3 times longer than that of the other models and the accuracy was improved by only 3%. The $k-\epsilon$ and $k-\omega$ models were roughly equivalent in their accuracy. Each model proved to be within 10% of the measured value prior to the void-fraction correction. It was concluded that the RNG $k-\epsilon$ model was most appropriate for this type of simulation.

Fernandes et al. compared the performance of CFD simulations to experimental studies separately involving ambient air and supercritical CO₂ under both laminar and turbulent conditions.²⁰ Turbulent simulations employed the realizable $k-\epsilon$ turbulence model. Empirical parameters were determined to account for the drag and permeability associated with the porous gauze packing. The first geometry simplified the SULZER EX gauze packing as two contacting corrugated sheets. Velocity inlet (bottom) and pressure outlet (top) conditions were specified. The average deviation of the pressure drop for the supercritical CO₂ flows was 15%. The second geometry approximated a single packing element with an outer diameter of 24 mm. This packing-element model was able to predict the dry pressure drop with an average deviation of 6%. Each geometry employed a tetrahedral mesh with a 0.31-mm minimum element size. Hexahedral meshing was attempted but abandoned because of unavoidable low mesh qualities.

In 2008, Fernandes et al. extended their study to address liquid film flow.²¹ An Euler–Euler approach was combined with the volume-of-fluid (VOF) multiphase model. Two models were employed. Two-dimensional liquid film flowing down a corrugated

surface was modeled first to obtain approximations of film thickness. This information was then employed to generate a three-dimensional geometry with periodic liquid in- and outflow boundary conditions. Simulation predictions were found to accurately capture the trends of pressure drop as a function of flow rate. The relative errors for the pressure drop calculations were 20.3% for dry conditions and 23% for irrigated conditions. The authors hypothesized that these errors were due to uneven gas and liquid distributions, lack of flow channeling, and lack of liquid back-mixing predicted by the model. Calculations of the height equivalent to a theoretical plate (HETP) had a relative error of 9.15%. The errors were attributed to the assumption of uniform distributions in the liquid and vapor phases.

In the described research, simulations were conducted with approximations to the actual geometry. The results showed that CFD can be used in lieu of experimentation to develop predictive models of contactor performance. However, this method of simulation is inherently dependent on empirical fitting and, therefore, cannot provide a rigorous analysis or predictive model of column performance or be used for computer-aided design of next-generation contacting media.

Modeling of constitutive geometry elements restricts study to small-scale, local phenomena. Because the subsets are modeled independently, any analysis of distribution, holdup, or wetted area is precluded. The need to model the subsets independently also introduces error as adjacent geometries display complex interaction that cannot be taken into account a priori. As in the research of Mahr and Mewes, geometry approximations can be used to predict column-scale performance. However, the approximations require extensive fitting and are valid only for the specified packing design. To analyze the complex interactions of column-scale variables and local transport phenomena, simulations must use accurate geometries modeled in their entirety.

METHODS

Geometry Generation. X-ray computed tomography (CT) scans were used to quickly obtain a high-fidelity electronic representation of a structured packing. In X-ray CT, the transmittance of X-ray beams through an object is measured from many different projection angles as the object or emitter/detector pair is rotated (see Figure 1). X-ray attenuation is roughly

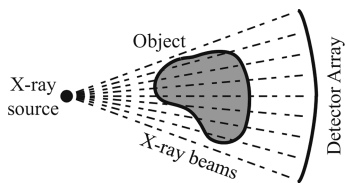


Figure 1. Overhead view of a fan beam and linear array X-ray detector.²³

proportional to density. Therefore, each scan corresponds to the superposition of all of the densities along the beam's path. The purpose of taking scans from multiple angles is to obtain many unique beam paths. This allows deconvolution algorithms to regress the density at each point. The result is typically displayed as a three-dimensional density map of the scanned object. X-ray CT is a nondestructive testing technique in that it allows one to see inside an object without the need to physically alter the object.

A 450 kV, 1.3 mA unfiltered fan X-ray beam was paired with a 512-channel cadmium tungstate solid-state linear array detector to perform all CT scans. A single beam captured one sample per view with an integration time of 20 ms, and each rotation was

repeated with a half-detector offset to double detector coverage, improving image resolution. Slice thicknesses were 0.3125 mm, with an interslice spacing of 0.3 mm. For each slice, 1400 views (angular positions) were used. The source-to-object distance was 752 mm, resulting in a 159.24 mm maximum field of view.

Ring artifacts were removed using the IDL (Interactive Data Language) routine RK_SinoRingProcSimul developed at the University of Texas.²² Reconstruction utilized beam hardening coefficients of [0 0.6 0.05 0.05]. Reconstruction parameters were set so that air had mean value of 10 000 and other materials maximally filled the available 16-bit data space (i.e., 65 536 possible data values). The scan and postprocessing yielded 547 512 × 512 16-bit TIFF slice images. These images were converted to an STL (stereolithography format) file using VGStudioMax 2.0. The threshold was set at 19 026 with superprecise quality and no simplification.

The goal of this research was to model a stack consisting of three distinct packing elements, capturing both the physics at the joint as well as the midpacking regions and the transitions between the two over the course of a packing stack. Therefore, the central 154.87 mm of a half-element of Mellapak N250Y was scanned in the manner described previously. The STL file was imported into ICEM CFD mesh-generation software for manipulation. The scan intentionally ignored the first and last millimeter of packing to create a flat plane perpendicular to the packing axis. Figure 2 shows the results of the packing-element scan without a containing geometry.

The imported scan data were copied, translated along the Z axis, and rotated by 90°. This procedure was then repeated with the copied data to create three packing elements such that the second element was rotated by 90° and the third element was rotated by 180° relative to the first element. This is shown in Figure 3. The base of each element was spaced 0.01 mm from the end of the previous element to prevent contact errors. This gap was also small enough that the intended mesh size would not resolve the space.

The geometry had to be saved in an open format readable by Star-CCM+. The STL file format was chosen for consistency. The geometry generated in ICEM is of the type B-spline and had to be converted to a faceted geometry format. The faceted and triangulated STL geometries were then merged and converted to an unstructured mesh. This allowed the export of a single STL file representing the combined geometry.

Meshing. The combined-geometry STL file was imported into Star-CCM+ for meshing. At this point, the geometry was not water-tight and did not have a surface discretization appropriate for CFD analysis. To obtain a water-tight surface sufficient for CFD meshing and subsequent analysis, a surface wrapping technique available in STAR-CCM+ was used to wrap the STL surface geometry. This process fills holes and gaps below a minimum desired length scale and eliminates duplicate data and internal features. The surface wrapper also generates an unstructured mesh aligned to the surface, which results in a mesh that can be employed in CFD while still retaining the original CT accuracy subject to any user-supplied minima. Leak detection was performed on both the flow volume and packing internal volumes after running the surface wrapper. All volumes were found to be water-tight and suitable for meshing.

The surface remesher, tetrahedral mesher, and polyhedral mesher routines were invoked serially to generate the final volume mesh. Because an STL file utilizes triangulated surfaces, a surface mesh was already present on the imported data. This mesh was based on the resolution of the CT scan, however, and

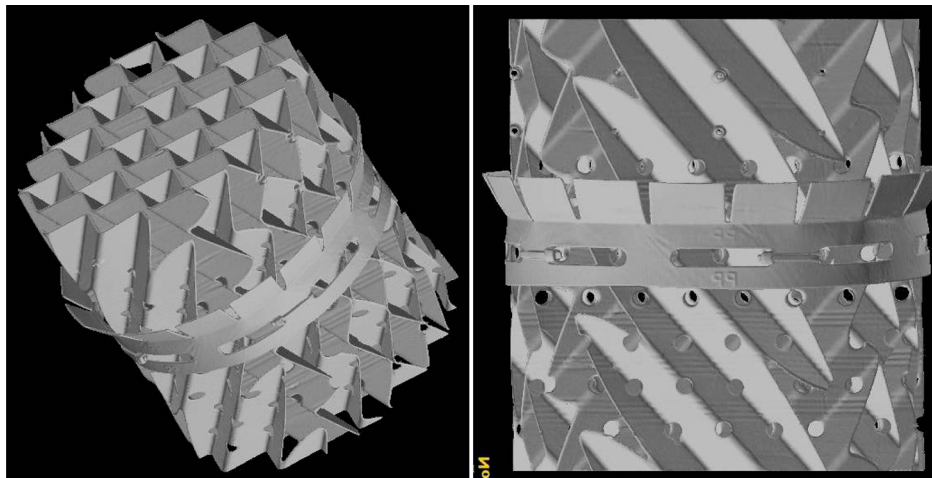


Figure 2. Geometry (left, isometric view; right, side view) generated by scanning a single half-element of Mellapak N250Y.

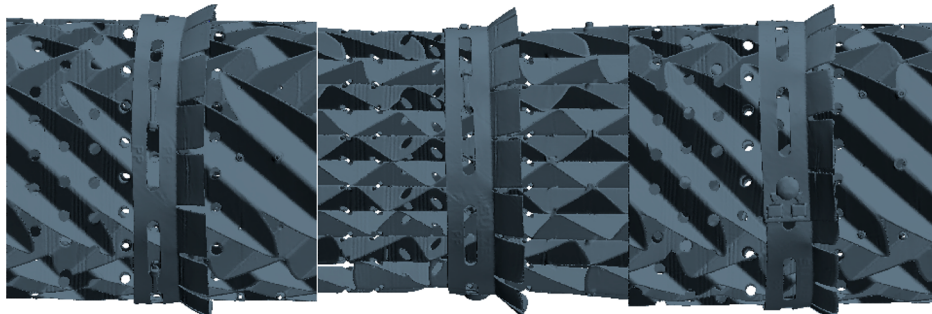


Figure 3. Packing stack consisting of three half-elements of Mellapak N250Y.

did not represent a clean or well-defined set of surfaces. CFD simulation with this original mesh would likely have failed because of the poor quality. Therefore, the surface remesher was used to overwrite this low-quality mesh with one expressly suited to CFD calculations. Most CFD studies generate a volume mesh by extrapolating a triangular surface mesh to form pyramidal or tetrahedral volume elements. The downside to rigidly enforcing a four-sided volume element is that these volumes can become highly warped or skewed when describing the volume between or near highly angular surfaces. This difficulty has given rise to a new meshing method that employs many-sided or polyhedral volume elements. The polyhedral elements can be packed more efficiently into acute spaces without becoming misshapen. Another benefit is realized by merging adjacent tetrahedral volumes to form a single polyhedral volume. Merging adjacent pyramidal shapes results in a minimal increase in edge length while reducing the mesh volume count by a factor of 2 or more. This allows polyhedral meshes to converge in fewer iterations than the tetrahedral equivalent without sacrificing accuracy. The reduction in volume elements required by polyhedral meshes also results in a much smaller file size.

The size and complexity of the constructed geometry prevented the use of a uniformly spaced mesh. Therefore, adaptive meshing was employed to generate a mesh with the requisite accuracy while minimizing the file size and computation time. This process allows the user to specify global limits on parameters such as maximum or minimum mesh element size, cell growth rate, or minimum mesh quality. The software then autonomously generates a relatively simplistic mesh throughout the geometry. Once a complete mesh is present, the software

proceeds to step through the existing mesh and refine the grid spacing. The mesh is iteratively refined on the basis of the specified parameters as well as geometric complexity. A more detailed mesh is required to accurately capture complex flow fields. Therefore, the adaptive meshing algorithm refines the mesh based on the distance to walls and local geometry density or surface curvature to capture important geometric and flow-field features.

This study generated three meshes to assess how the differing parameters would affect final mesh quality. The manipulated mesh variables consisted of the number of points to define a circle, the surface growth rate or growth factor, and the tetrahedral/polyhedral density. Requiring more points to define a circle increases the number of mesh vertices used to describe a given curve and results in a more accurate simulation of flow across or near curved surfaces. The surface growth rate controls the allowable edge length increase in adjacent surface triangles. A larger value results in a more sudden transition from fine to coarse areas within the surface mesh. The tetrahedral/polyhedral density parameter affects the global volume element density. That is, the total number of volume elements scales roughly linearly with this value. The tetrahedral/polyhedral growth factor functions in a manner similar to the surface growth rate, with the obvious caveat that it applies only to volume elements.

The minimum edge length was not changed between the meshes but deserves mention because it is the only absolute parameter that was specified. The minimum edge length is an inviolate restriction on the enhancements made by an adaptive meshing program. This study employed a minimum edge length of 0.45 mm in all three meshes and used the default values for the

remaining parameters in the first or coarse mesh. The medium and fine meshes changed these parameters such that they would have increased resolution compared to the coarse mesh. The parameters used in this study are summarized for each mesh in Table 1.

Table 1. Mesh Generation Parameters for Each Mesh

parameter	coarse	medium	fine
no. of points/circle	36	48	48
surface growth rate	1.3	1.2	1.1
minimum edge (mm)	4.5	4.5	4.5
tetrahedral/polyhedral density	1.0	1.0	1.05
tetrahedral/polyhedral growth factor	1.0	0.98	0.97

Meshing was performed on the Texas Advanced Computing Center (TACC) high-performance visualization cluster known as Spur. The coarse mesh was created on a standard visualization node. These nodes are equipped with four quad-core AMD Opteron processors, 128 GB of RAM, and one NVIDIA QuadroPlex 2100 S4 visual computing system (four FX 5600 graphics boards). The medium mesh required extra memory and was generated on the visbig node, which is equipped with eight dual-core AMD Opteron processors, 256 GB of RAM, two NVIDIA QuadroPlex 1000 Model IV visual computing systems (two FX 5600 graphics boards each). These meshes were generated in a runtime of less than 24 h. The fine mesh was also generated on the visbig node but required a runtime of 30 h.

Simulation. CFD simulations were conducted using Star-CCM+ on the TACC high-performance computing (HPC) cluster known as Ranger. Ranger contains 3936 computer nodes, each of which is equipped with four quad-core AMD Opteron processors and 32 GB of PC2-5300 RAM. Intranode communication is conducted by HyperTransport lanes between each of the four sockets, whereas internode communication is supported over a dedicated, high-speed, low-latency InfiniBand network. Simulations were conducted using 480–544 cores (30–34 nodes).

Star-CCM+ supports the following turbulence models: Spalart–Allmaras, Reynolds stress, k –omega (k – ω), and k –epsilon (k – ε). The Spalart–Allmaras model uses a single independent closure equation and was judged to be too simple for the detailed analysis desired in this research. The RSM occupies the other end of the spectrum, using an independent equation to calculate each additional term in the Reynolds-averaged Navier–Stokes (RANS) equations. This model is widely regarded as the most accurate commercially available turbulence model; however, it suffers from excessive computation time and is often used only as a comparative point to evaluate other models. The k – ε and k – ω models each use two independent equations for closure and are very popular in the CFD field. A literature search showed that the k – ε model and its derivatives are more commonly employed when studying chemical engineering flow applications.

Many improvements have been made to the k – ε turbulence model since its original formulation. One much-lauded improvement is the realizable approximation. The realizable k – ε model uses an improved equation to calculate the turbulent dissipation rate, ε .²⁴ The realizable model also expresses the C_μ coefficient as a function of the mean flow in lieu of keeping it constant as in the standard k – ε model.²⁴ The realizable k – ε model is typically expected to give results as accurate as or better than those of the standard application for most flows.

A second common improvement is the use of two-layer theory, which allows the k – ε model to be applied in the viscous sublayer,

thereby negating the need for wall functions.²⁴ This is accomplished by modeling ε differently based on the distance from the wall. In the layer adjacent to the wall, the turbulent viscosity (μ_t) and ε are specified based on the distance from the wall. However, ε is computed from the transport equation at points far removed from the wall. These values are blended in the intermediary region. Because of the complexity of the flow and the significant surface area exposed to the fluid, this research employed the two-layer realizable k – ε model. A single flow simulation was repeated with each the k – ω model and the RSM to judge the wisdom of this choice.

Initial simulation efforts modeled nitrogen as a steady, incompressible flow using a segregated solver. A segregated solver calculates the velocity and pressure terms independently of one another. This allows for more ambitious iteration steps and quicker convergence. Unfortunately, this solution method proved unstable. Next, a coupled solver was used to model the flow as constant in density. This method proved very robust and arrived at a solution for all flows.

The simulation with the lowest flow rate was initialized with a constant velocity and pressure profile. Subsequent simulations were initialized from the converged solution of a previous flow rate. In each iteration, the area-weighted average pressure was calculated in a plane 25.4 mm below the packing stack and in a second plane 25.4 mm above the packing stack. These values were used to calculate pressure loss across the stack, which was, in turn, used to monitor convergence. All simulations were run until the pressure loss changed by less than 0.001 Pa between subsequent iterations.

Distillation vapor rates are commonly referred to in terms of the F factor (F_S). This is defined as the product of the superficial linear velocity and the square root of the vapor density

$$F_S = u_G(\rho_G)^{1/2} \quad (1)$$

As a general rule, columns are prone to flooding above F factors of $2.4 \text{ (m/s)}(\text{kg/m}^3)^{1/2}$.

Simulations were conducted at $F_S = 0.610, 1.22, 1.83, 2.45$, and $3.05 \text{ (m/s)}(\text{kg/m}^3)^{1/2}$. The entering flows were specified as a mass flow rate at the suggestion of the CFD software vendor. This is in contrast with many CFD studies, which specify the linear velocity flux through the inlet boundary. The use of a total mass flux enables the software package to adjust the local flux across the inlet boundary while maintaining the same superficial flow rate. One advantage is the extra degree of freedom presented at the intersection of the inlet boundary and the no-slip boundary conditions imposed at the column wall. The result is a more representative flow profile at the inlet.

Experimentation. An experimental campaign was conducted to obtain data against which simulation predictions could be validated and to quantify the effect of packing joints on pressure loss. All experiments measured the pressure loss of single-phase flow against gravity through plastic Sulzer-brand packing with a specific area of $250 \text{ m}^2/\text{m}^3$ (commonly referred to by its model ID, Mellapak N250Y). Each packing element had perforations, a single wiper band, and surface enhancement.

In total, this project studied three distinct packing configurations (three half-elements, four half-elements, and two whole elements). In each experiment, the system was brought to a steady flow, and the pressure loss was recorded. The experimental order was random and included two duplicate runs of each flow rate. The average pressure loss of each individual run was used for comparative analyses.

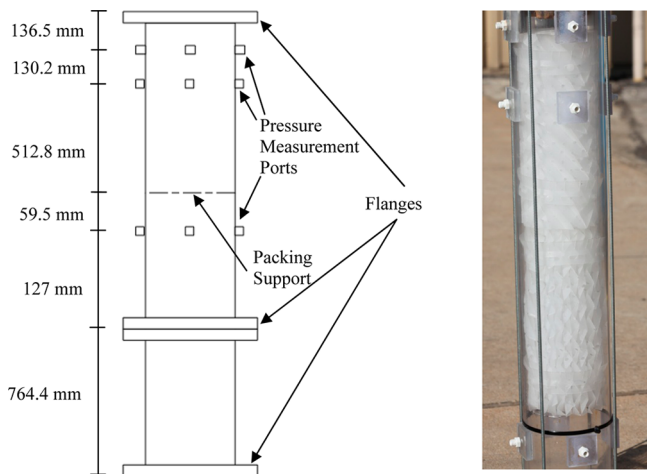


Figure 4. (Left) Schematic and (right) photograph of the column.

Equipment. Column. The column (depicted in Figure 4) was assembled from a cylindrical aluminum base and two sections of 146.05-mm-i.d. polycarbonate tube. The base had a 33.4-mm [1-in. National Pipe Thread taper (NPT)] threaded process connection drilled perpendicular to its axis. This connection intersected a conical throat drilled along the central axis of the base. The throat was 76.2 mm in diameter at its top and 25.4 mm in diameter where it intersected the process connection. The flaring of this channel was meant to facilitate a more uniform flow distribution as the fluid entered the column.

The lower tube section was 764 mm tall and acted as a spacer in which the flow profile would develop prior to encountering the packing. The upper tube section was 966 mm tall. Pressure ports were installed in the upper section of tube at elevations of 127, 699.3, and 829.5 mm above the flanged tube connection (see Figure 4, left). At each elevation, four ports were spaced evenly around the column perimeter in a plane perpendicular to the column axis. A picture of the column, packed with two whole-elements of Mellapak N250Y is shown on the right in Figure 4. All three pressure-measurement elevations are clearly visible in this figure.

Packing Support. The packing was supported 186.5 mm above the intersection of the polycarbonate tubes. Four holes were drilled, and a single wire was fed from one side of the column, through the opposite wall, around the exterior of the wall, back into the column, and out through the last hole (see Figure 5).



Figure 5. Packing support wire.

The wire was secured by compressing the tag ends to the column wall with vinyl strapping. The holes in the column wall were sealed with silicon sealant. This configuration provided minimal extraneous material to create drag or separation points to disrupt flow.

Flow Configurations. Experiments were conducted with a single-pass flow of building-supplied nitrogen. All piping was flexible 38.1-mm (nominal 1.5-in) schedule 40 poly(vinyl chloride) (PVC). Nitrogen flow was fed to the system from wall-mounted taps. A ball valve was installed at the tap and used to manually control flow. From there, the flow was split and fed through two mass flow meters in parallel to reduce pressure drop and allow the study of higher flow rates. The flow was recombined after the meters and carried to the base of the column. Nitrogen flowed through the column and was then vented to the atmosphere. This configuration is diagrammed in Figure 6. The nitrogen temperature

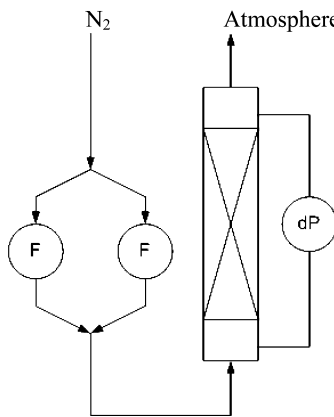


Figure 6. Flow diagram for the experimental apparatus.

was monitored and found not to vary outside the range of 22.3–23.9 °C. This roughly corresponds to room temperature, and the thermal stability likely reflects a long residence in the nitrogen headers inside the climate-controlled portion of the building.

Instrumentation and Data Acquisition. The process flow was run in parallel through two MicroMotion F50 flow meters. Pressure loss was measured with four MKS 226A differential pressure sensors measuring the pressure loss across the packing stack. A National Instruments USB-6008 data acquisition card was used for process monitoring. All instrumentation in this study used a 4–20-mA signal based on the scaled flow value. The current signal was preferred because it is not sensitive to electromagnetic interference commonly found in industrial buildings. The current signal was converted to a 1–5-V dc signal by placing a high-accuracy ($\pm 0.1\%$) 250-Ω resistor in the current loop.

Procedure. Pressure loss measurements were taken across three packing stacks (three half-elements, four half-elements, and two whole-elements of Mellapak N250Y) at nitrogen flows of $F_S = 0.610–3.36 \text{ (m/s)}(\text{kg/m}^3)^{1/2}$. The specific flows are compiled in Table 2. Each experiment followed a randomized list of flow rates that included two duplicate runs. The lowest-pressure ports were used as the high leg for all ΔP measurements. The middle-pressure ports were used as the low leg when studying flow through three half-elements, whereas the highest-pressure ports were used as the low leg when measuring pressure drop through two whole elements and four half-elements. Any ports not in use were capped.

A 9.525-mm ball valve at the wall was used to control the flow rate of nitrogen through the system. Prior to experimentation, the data acquisition virtual instrument was initiated to allow the user to monitor both flow and pressure drop. The flow was brought to the desired value and monitored to ensure flow stability. Data recording was initiated once the system was judged to be stable for a period of at least 3 min. Data were recorded for 3 min, and then the procedure was repeated at the next flow rate.

Table 2. Summary of the Nitrogen Flows Studied

<i>F</i> factor, <i>F</i> _S (m/s)(kg/m ³) ^{1/2}	(ft/s)(lb/ft ³) ^{1/2}	velocity, <i>u</i>	
		m/s	f/s
0.610	0.5	0.570	1.87
0.915	0.75	0.855	2.81
1.22	1	1.14	3.74
1.53	1.25	1.43	4.68
1.83	1.5	1.71	5.61
2.14	1.75	2.00	6.55
2.44	2	2.28	7.48
2.75	2.25	2.57	8.42
3.05	2.5	2.85	9.35
3.36	2.75	3.14	10.3

RESULTS AND DISCUSSION

Discrete Solutions. The underlying Reynolds-averaged Navier–Stokes (RANS) partial-differential equations describe from first principles fluid behaviors that are continuous in both time and space. Unfortunately, for engineering flows and complex geometries, closed-form analytic solutions of these governing equations are not available, and CFD uses numerical methods to generate discrete solutions that can be either transient or steady-state. Popular spatial discretization methods include finite-difference, finite-volume, and finite-element techniques, which each make different approximations to the governing equations so that they can be applied to discrete volumes.

The use of finite-difference schemes (or more advanced finite-volume schemes in the present case) imparts many advantages to fluid dynamics modeling. The greatest advantage is the ability to iterate toward an accurate representation of the flow field, subject to discretization approximations and modeling. The governing equations enforce a relationship among velocity, pressure, and fluid properties that can be iterated to achieve a steady-state solution for a given flow rate and packing configuration.

The selection of specific points within the geometry volume, called gridding or meshing, serves multiple purposes. Iterating to arrive at a solution requires the same points be used to advance the solution. Perhaps more important is the effect of the selection of these points on the required computing memory and the final solution accuracy. The error is on the order of the first truncated term in the difference scheme.

Unfortunately, closely spaced points also increase the memory needed to store iterations and the overall number of calculations needed per iteration. The conflicting needs of accuracy and expeditious simulation have led to the use of nonuniform grid dimensions. A highly refined mesh is used near geometry features that are likely to create sharp gradients in the flow field. The mesh points are spaced farther apart as the mesh grows into areas where the flow is expected to change more gradually. The texts by Thompson et al.²⁵ and by Durran²⁶ are recommended for further discussion of these topics.

Geometry. The CT geometry was scanned in just over 5 h, whereas reconstruction took approximately 2 h. The resulting STL file contained 5 439 254 triangles which occupied 251 MB when written with binary encoding. The ICEM-created geometry proved to be water-tight and easily imported into third-party programs when exported as an STL file. The process of scanning, modifying, and exporting the geometry in a format readable by the CFD meshing program proved more accurate, expedient, and economically preferred when compared to quotes obtained for computer-aided drafting (CAD) generation of the same geometry.

Meshing. The meshing methods outlined in the Methods section resulted in meshes with 35, 50, and 57 million polyhedral cells. In each instance, the conversion to a polyhedral mesh resulted in an 80% or greater reduction in cell count relative to the corresponding tetrahedral mesh. The data also suggested that mesh-size reduction was slightly more efficient in larger meshes. The polyhedral meshes resulted in file sizes between 18 and 30 GB. By contrast, the estimated file size for similar tetrahedral meshes would be between 200 and 340 GB using the common assumption of 1 GB per 1 million tetrahedral cells. These data are compiled in Table 3.

Table 3. Summary of the Characteristics of Various Meshes

parameter	coarse	medium	fine
tetrahedra	2.00×10^8		3.38×10^8
polyhedra	3.49×10^7	5.04×10^7	5.74×10^7
file size (Gb)	18.3	19.2	27.1
reduction in cell count	82.5%		83.0%

The increased cell count of the tetrahedral meshes would significantly increase the computational complexity and, therefore, the time required to reach a converged solution. Similarly, the file size corresponds to a minimum amount of RAM required to open a file. Most HPC clusters assign available RAM relative to the number of processing cores requested. Therefore, the much larger tetrahedral meshes would necessitate significantly more processors to perform the needed calculations.

The precision of a given mesh can only truly be measured by comparing results of simulations employing that mesh against those taken from analogous experimentation, whereas its accuracy can be assessed by repeated uniform mesh refinement. In practice, the relative suitabilities of varying meshes are often evaluated by analyzing certain quality metrics, such as face validity and volume change. Face validity is an area-weighted measure of the degree to which central cell-face normal vectors run parallel and away from their attached cell centroid.²⁴ Face validity below 0.5 indicates negative-volume cells. A preponderance of these cells infers a poor-quality mesh, either locally or globally.

All three meshes reported uniformly high face-validity metrics, with no mesh having any cells with face validity below 0.8448. The medium mesh could be judged to have the highest-quality faces, as no face had a quality below 0.957 and only a very small percentage of the faces fell below 1.0. The coarse mesh is of the lowest quality when judged by the percentage of faces with a quality below 1.0. The fine mesh was responsible for the lowest face quality; however, it also had the lowest percentage of face qualities below 1.0. These results are summarized in Table 4.

Table 4. Face Quality Statistics for Each Mesh

face validity	no. of cells		
	coarse	medium	fine
validity = 1.00	34 860 691	50 360 527	57 392 387
1.0 > validity \geq 0.95	892	785	381
0.95 > validity \geq 0.90	34	—	4
0.90 > validity \geq 0.80	1	—	2
0.80 > validity \geq 0.70	—	—	—
minimum	0.8772	0.9571	0.8448

The increase in the percentage of faces with quality equal to 1.0 corresponds to increased cell density and decreased cell growth

rate. This enforces a smoother transition from fine to coarse cells in the volume and results in a higher packing efficiency. The higher efficiency reduces the need both for misshapen cells to bridge gaps between cells with disparate sizes and for large cells to be situated near complicated surfaces.

The fine mesh performed much better as judged by the volume change metric (Table 5), having both the highest percentage of its

normally indicative of poor mesh regions. However, a single cell with this poor quality will have limited impact on the overall mesh quality and can be ignored.

Figure 7 shows the packing geometry without the wall bisected by the XY plane with the front portion removed. In this figure, Z increases to the right. Figure 8 shows the mesh elements that lie in the plane used to perform the cut in Figure 7. Samples of the coarse (Figure 8, top), medium (Figure 8, middle), and fine (Figure 8, bottom) meshes are shown. Although this is not a complete picture of the meshed volume, it is reasonably assumed to be a representative sample.

The coarse mesh (Figure 8, top) is modestly refined around the in- and outflow boundaries. The mesh grows quickly, and large elements can be seen in the open region prior to and immediately downstream of the packing stack. The mesh transitions very abruptly to a highly refined mesh near the beginning (190 mm) and end (655 mm) of the packing. The mesh is noticeably nonuniform throughout the packing stack. The mesh is relatively coarse in the intervals 267–345 and 423–500 mm. These increases in mesh size likely correspond to areas with higher local void fractions in which the high cell growth rate permits a rapid increase in cell size over a small distance.

The medium mesh (Figure 8, middle) is similar to the coarse mesh in the open volumes prior to and following the packing but is much more refined within the packing volume and near the wall adjacent to the packing. The mesh is visibly more densely packed in the first half of the packing elements (e.g., 190–267,

Table 5. Volume-Change Metrics for Each Mesh

volume change	no. of cells		
	coarse	medium	fine
$1 \times 10^{-1} \leq \Delta V \leq 1 \times 10^0$	34 172 904	49 813 616	57 017 289
$1 \times 10^{-2} \leq \Delta V < 1 \times 10^{-1}$	670 003	534 947	364 410
$1 \times 10^{-3} \leq \Delta V < 1 \times 10^{-2}$	18 504	12 579	10 981
$1 \times 10^{-4} \leq \Delta V < 1 \times 10^{-3}$	196	154	86
$1 \times 10^{-5} \leq \Delta V < 1 \times 10^{-4}$	11	15	8
$1 \times 10^{-6} \leq \Delta V < 1 \times 10^{-5}$	—	1	—
$1 \times 10^{-7} \leq \Delta V < 1 \times 10^{-6}$	—	—	—
minimum	1.22×10^{-5}	3.17×10^{-6}	2.15×10^{-5}

cells in the highest-quality range and the highest minimum volume change. Once again, the coarse mesh had the highest percentage of cells outside the top-quality range but was not responsible for the lowest volume change of the three. The medium mesh had the lowest volume change and was the only mesh to have a cell volume change below 1×10^{-5} . Multiple cells below this threshold are

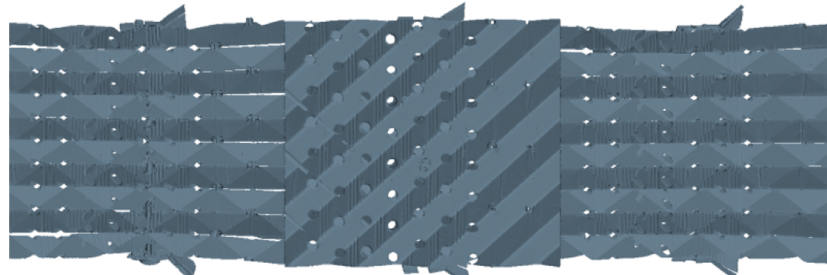


Figure 7. Packing geometry shown with the front section cut away by the XY plane and along the central (Z) axis.

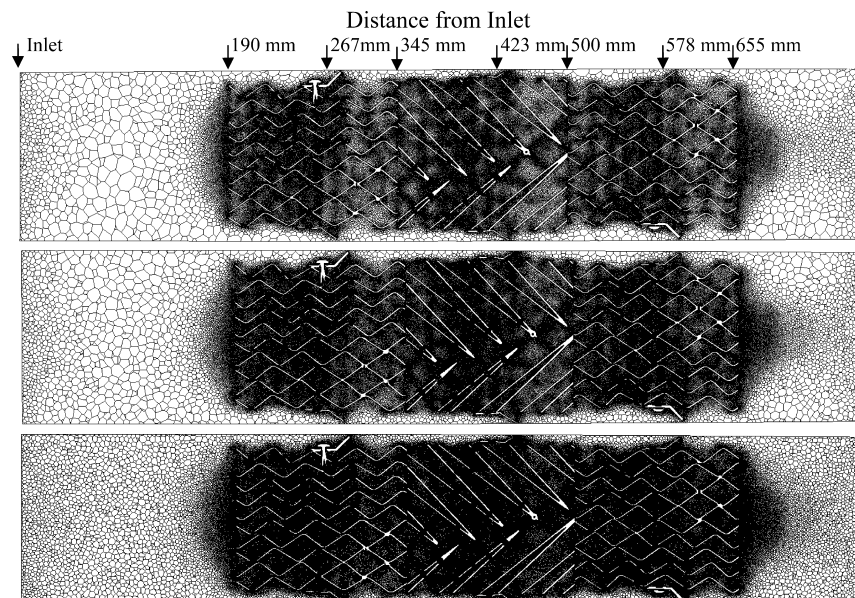


Figure 8. Coarse (top two), medium (middle two), and fine (bottom two) meshes created to assess the effects of mesh resolution on the final solution.

345–423, and 500–578 mm). The mesh still coarsens throughout the second half of each packing element, as was seen in the coarse mesh. The resulting mesh is still more highly refined than the coarse mesh in these areas. For these reasons, it would be appropriate to think of the medium mesh as being more refined than the coarse mesh within the packing volume and largely equivalent elsewhere.

The fine mesh (Figure 8, bottom) is much more refined throughout than either the coarse or medium mesh. There is negligible coarsening as it transitions between the in- or outflow boundary and the open volume. The volume within the structured packing seems almost uniformly meshed, with very few pockets of slightly coarser meshing near the end of each packing element. The annular volume between the packing and column wall is also described by a much finer mesh than in the previous meshes. This mesh could be viewed as an upper limit on the resolution of a mesh with 0.45-mm minimum element sides.

Grid Sensitivity. A final step in evaluating mesh performance is to conduct identical simulations with different mesh sizes to assess how the mesh resolution affects convergence. Steady-state simulations were conducted with each mesh using a coupled solver and two-layer realizable $k-\epsilon$ turbulence modeling. Transient simulations were also conducted with the fine mesh to test for the presence of any time-variant phenomena that the steady simulations could not capture. These results are presented in Figure 9.

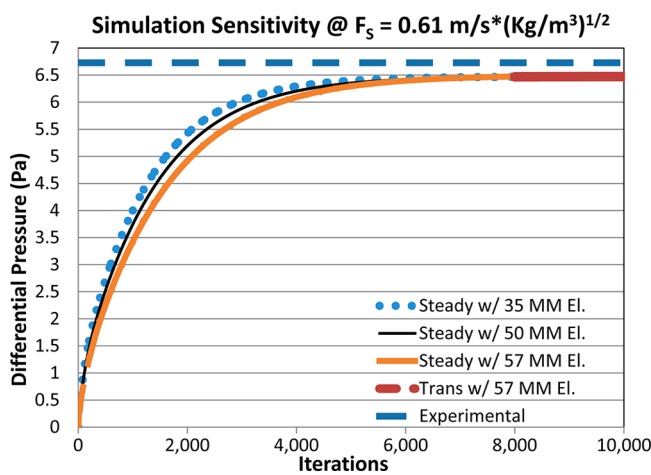


Figure 9. Nitrogen simulations of $F_S = 0.61 \text{ (m/s)}(\text{kg/m}^3)^{1/2}$ performed with each mesh file converged to the same value.

All three mesh resolutions converged to the same predicted pressure loss across the packing stack. The use of subdivided volumes necessarily results in an averaging of the flow phenomena across the chosen volumes, often resulting in small errors that accumulate across the mesh volume. Therefore, it is expected that more highly refined meshes will yield more accurate answers. This accuracy comes at the expense of computational time, as the increased number of cells in fine meshes requires more computations.

The equivalent solutions of the coarse and fine meshes are encouraging, indicating grid convergence for the quantities of interest. The smallest mesh typically converged in 2000–4000 fewer iterations than the largest mesh. This means that analyses for macroscopic variables, such as pressure drop, can be calculated very quickly with relatively coarse meshes without sacrificing accuracy. More localized values such as streamlines

and velocity vectors might require the higher spatial accuracy of a more refined mesh. The desire to study such values was the rationale behind using the highly refined mesh throughout this study.

Steady-state simulations employ a number of approximations to obtain approximate, time-averaged solutions. One such approximation is the use of local time steps, which are dynamically adjusted to obtain essentially invariant behavior.²⁴ Obviously, the use of steady simulations is inappropriate to flows that have periodic boundary conditions or otherwise changing flows. However, unsteady phenomena are sometimes present in steadily imposed flows. An excellent example is the vortex shedding that occurs in flow around a sphere above a critical Reynolds number. The possibility of such behavior requires that a transient simulation be conducted even when a steady flow is expected.

To this end, a transient simulation was performed with the fine mesh using the same turbulence settings as in the steady simulations. Default transient settings were employed for this first analysis. As can be seen in Figure 9, the transient simulation did not deviate from the results obtained from the steady simulations. This suggests there were no large-scale transient phenomena and that steady simulations should be sufficient to obtain a gross understanding of the prevailing physics in the continuous phase of this structured packing. This should not be taken to mean that no transient phenomena occur or that transient simulations would not be useful in analyzing structured packing. There might well be offsetting time-variant phenomena that do not affect macroscopic pressure performance but could prove instrumental in improving local pressure dissipation or, in the long run, mass transfer.

Investigating this possibility would require a great deal of trial and error to optimize the transient constants and choice of time step. The goal of this work was to obtain a macroscopic representation of flow through structured packing not the identification and modeling of transient phenomena that do not affect the overall pressure drop results. Therefore, further time-variant investigations were not pursued.

Turbulence Modeling. The evaluation and selection of appropriate turbulence models is also of great importance when conducting CFD simulations. Therefore, the performances of the $k-\epsilon$ and $k-\omega$ models are compared in Figure 10. The

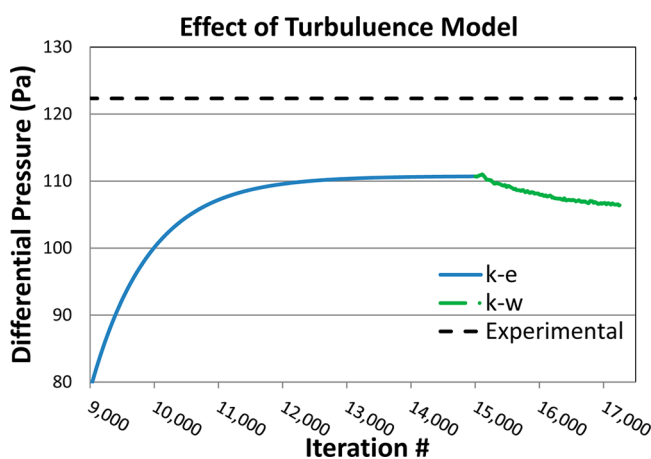


Figure 10. Comparison of the performance of different turbulence models at a flow of $F_S = 3.05 \text{ (m/s)}(\text{kg/m}^3)^{1/2}$.

solution was initialized by assuming a uniform velocity field and then solved with a steady-state, two-layer realizable $k-\epsilon$

turbulence model. As can be seen in the figure, the computations were allowed to run until well past a steady solution. The $k-\epsilon$ model converged at a value approximately 9% below the experimentally predicted value. This solution was then used as the starting point for the $k-\omega$ model. The predicted pressure drop began falling immediately upon switching the turbulence model. The simulation was stopped after the predicted pressure drop fell 4% below the already inaccurately low prediction of the $k-\epsilon$ model. This procedure was then repeated with the RSM.

Simulations using the RSM diverged after only 96 additional iterations, during which the overall pressure drop increased at a precipitous rate. The RSM is a very complex calculation with many more constants than the two-equation models mentioned previously. Therefore, the RSM was restarted from the converged $k-\epsilon$ solution without the effect of gravity and with the energy equation turned off, under the belief that a simpler calculation might prove more stable. Surprisingly, the RSM diverged again after only 10 iterations with these parameters removed. The observed instability is likely a result of attempts to use the default parameters to simulate flow through a very complicated geometry. Clearly, the default parameters are not suitable for simulation of flow through the studied structured packing. However, finding the correct combination of so many parameters is likely to be a time-consuming undertaking. By comparison, the robust nature of the two-equation models means they will nearly always converge. The parameters can then be fine-tuned to improve the accuracy. As will be shown below, the $k-\epsilon$ model proved to be highly accurate. Therefore, the RSM could only marginally improve the results, and it was decided that the effort would be better spent analyzing the results of simulations conducted with the two-equation models.

The bulk of the simulations were carried out with the two-layer realizable $k-\epsilon$ model. As shown in Figure 11, the simulation

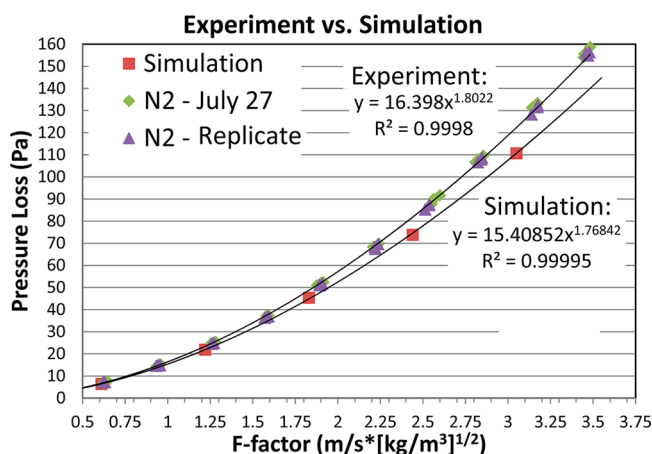


Figure 11. Comparison of experimental and simulation-predicted pressure drop.

predictions compared favorably with experimental results. On average, the simulations predicted a pressure drop 7.5% below the measured value. The accuracy was highest at the lowest flow rate, which predicted a pressure loss only 3.7% lower than experimental results. The error increased with increasing flow. When the correlations were extrapolated to $F_S = 3.66 \text{ (m/s)}(\text{kg}/\text{m}^3)^{1/2}$, the simulation correlation predicted a pressure loss that was 10.3% lower than the experimental correlation.

An inaccuracy in reproducing column diameter for use in the simulations is likely contributing to the underprediction of the

pressure loss by the CFD simulations. In the experimental column, the wiper bands were compressed when the packing was inserted, whereas the simulation wall was fit to the exterior diameter of the uncompressed wiper bands. However, the fact that the wiper bands do represent a periodic barrier to wall flow means that the bypass flow is limited to regions between the wiper bands. The high accuracy can likely be attributed to the wiper bands somewhat negating the effects of the increased annular area. It is not unreasonable to assume that repeated simulation with an accurate column diameter would prove even more accurate.

Among the goals of this project is the increased acceptance and application of CFD simulations for analysis and design of distillation contacting media. Therefore, the experimental and simulation results were compared to the Stichlmair model for calculating dry pressure loss through structured packings. The Stichlmair model calculates dry pressure loss as a function of void fraction, Reynolds number, fluid density, and packing-specific constants.^{12,27} The Mellapak N250Y-specific parameters are provided in Table 6.¹²

Table 6. Stichlmair Parameters for Plastic Mellapak N250Y Structured Packing¹²

parameter	value
$a (\text{m}^2/\text{m}^3)$	250
ϵ	0.85
C_1	1
C_2	3
C_3	0.35

The given Stichlmair parameters list the void fraction (ϵ) of Mellapak N250Y at 85%. This contradicts previous research that used X-ray CT to measure the void fraction of Mellapak N250Y in a 146-mm column and found it to be 91.6%.²⁸ However, even that value is inaccurate to describe Mellapak N250Y in a column with a simulation diameter of 159 mm. As a correction, the packing volume was calculated from Owens et al. and used as the occupied volume in the simulation geometry.²⁸ Combining this value with the simulation diameter allowed the calculation of the simulation void fraction. This value was calculated to be 92.9%. The measured and simulated pressure drops are presented alongside the Stichlmair predictions in Figure 12. The errors

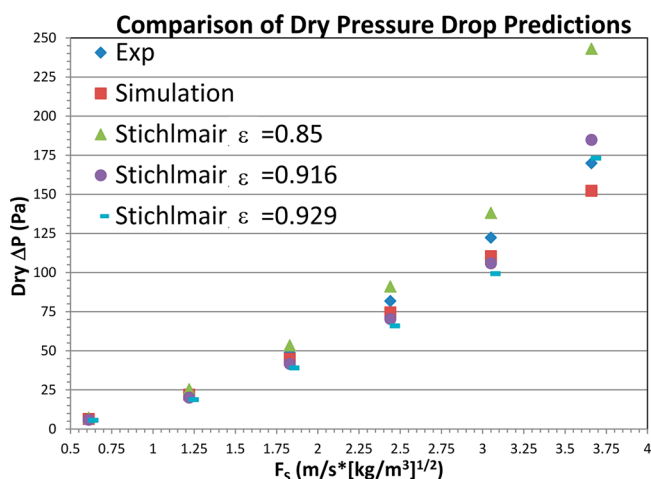


Figure 12. Comparison of predictions of dry pressure drop.

relative to experiment are shown in Figure 13 for both the simulation and Stichlmair predictions.

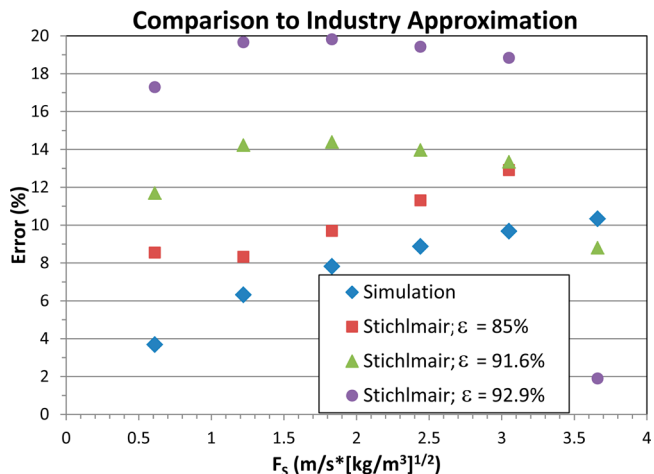


Figure 13. Errors of various dry ΔP predictions.

Overall, the simulation was more accurate than the uncorrected ($\epsilon = 0.85$) and both corrected ($\epsilon = 0.916$, $\epsilon = 0.929$) Stichlmair models, which gave average errors of 15.6%, 12.7%, and 16.2%, respectively. With the exception of one point, the simulation predictions show less error than either the uncorrected or corrected Stichlmair models. The simulation also more accurately conveyed the nature of the response to increasing flow rates. It is interesting to note that the uncorrected Stichlmair model actually outperformed both corrected models.

Diagnostic Analysis. The immense volume of data generated by CFD simulations is one of the many benefits of this method of study over traditional experimentation. Each flow quantity

present in the RANS solution is available at all discretized points in the volume and surface meshes. These values are given to a high precision without the need for expensive, complicated, or intrusive instrumentation. Moreover, the geometry of study does not need to be modified to include data-gathering devices.

Consider Figure 14 as an example. This figure shows the minimum and maximum velocity magnitudes in the Z (vertical) direction. The velocities are measured in planes that are perpendicular to the column axis at distances of 12.7, 25.4, and 38.1 mm up- and downstream of the beginning of the packing, each packing joint, and the end of the packing stack, as well as planes at the center of the wiper bands in each element. This enables a very thorough analysis of how the velocity distribution reacts as it travels through each subset of the packing volume.

Prior to entering the packing (150–190 mm), the velocity distribution was very narrow, and the minimum velocity was positive. Negative velocities were observed immediately after entering the packing. The maximum velocity necessarily increased at this point as the average velocity at any elevation must equal the superficial velocity. The wiper bands occluded the annular area and reduced the available cross-sectional area (CSA). The reduced CSA required that the linear velocity increase. This effect can be seen in the planes containing wiper bands at elevations of 268, 423, and 578 mm. The joints produced the opposite response. The magnitude of negative flow jumped dramatically at each joint (345 and 500 mm). Negative flows were no longer observed once the flow left the packing (655 mm); however, the velocity distribution was still larger than that prior to entering the packing.

This analysis was repeated for the area-weighted-average (AWA) pressure in the same planes, with the exception of the

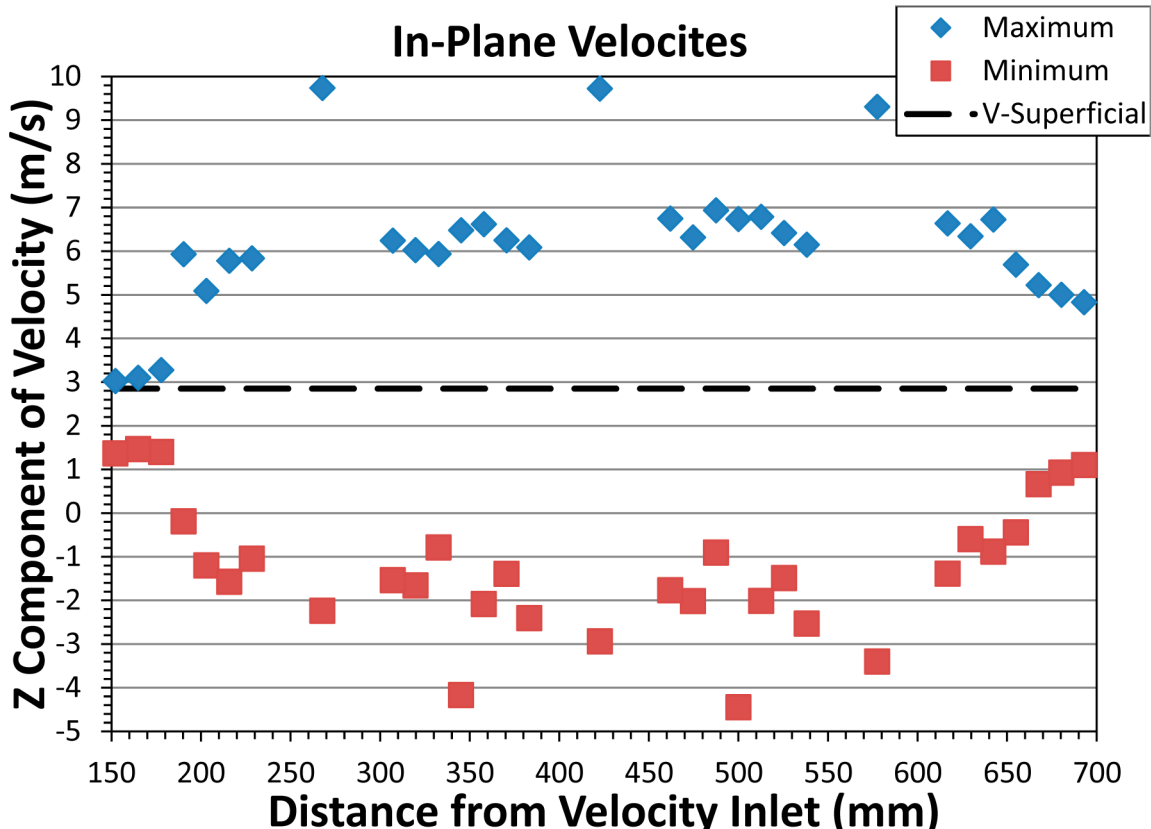


Figure 14. In-plane velocities calculated from the highest nitrogen flow rate. Wiper bands were located 268, 423, and 578 mm from the inlet; joints were at 345 and 500 mm; and the packing began and ended at 190 and 655 mm, respectively. The simulation was conducted at $F_s = 3.66$ (m/s) $(\text{kg}/\text{m}^3)^{1/2}$.

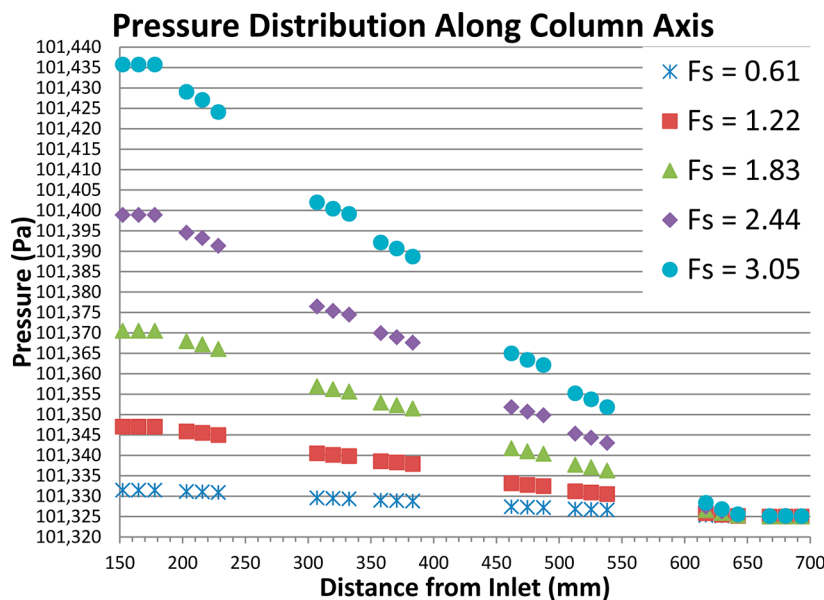


Figure 15. In-plane area-weighted average pressures calculated at various heights. Wiper bands were located 268, 423, and 578 mm from the inlet; joints were at 345 and 500 mm; and the packing began and ended at 190 and 655 mm, respectively. Units for F_S are $(\text{m/s})(\text{kg/m}^3)^{1/2}$.

wiper bands. These data are presented in Figure 15. The AWA pressure information proves informative as to how and where pressure is lost within the packing. Minimal pressure drop was observed prior to entering the packing. Because of increased surface area and skin drag, the pressure began to drop rapidly but smoothly as the flow progressed through the packing. In fact, the pressure drop appeared linear with progression along the length of the column for most of the packing. This linear relationship held true above and below the packing joint, but failed across the joint itself.

Taking the highest flow rate as an example, if a line were drawn through the three points above the joint and projected beyond the joint, it would predict a downstream pressure higher than observed. This shows that the joint caused a negative step change in pressure as flow proceeded through it. In quantitative terms, the 12.4 mm above and below each joint accounted for 10% of the packing length. However, this region contributed 12.6% of the pressure loss in the highest-flow simulation.

The joint's disproportionately high contribution to pressure drop was also observed experimentally. The pressure loss as a function of flow rate was measured through 610 mm of packed height using first half-elements (three joints per 610-mm height) and then whole elements (one joint per 610-mm height). The addition of two joints resulted in a noticeably higher pressure loss. This result is shown in Figure 16.

Although it might be argued that the additional pressure demonstrated in Figures 15 and 16 is negligible, these results must be viewed in the context of the distillation industry. These results specifically address single-phase flow, whereas distillation is a two-phase operation. Research conducted by Green et al. documented increased liquid holdup at, and just above, the joints in a two-phase contacting column using Mellapak M250Y.²⁹ This increase in liquid volume would consequently reduce the CSA available for gas phase flow and exacerbate the poor pressure performance at the joint discussed above. These results can be further combined with those of Owens et al., who observed large-scale recirculation and stagnation in bulk phase flows at the packing joint.²⁸ All of these observations suggest that the joints contribute disproportionately to pressure loss and promote back-

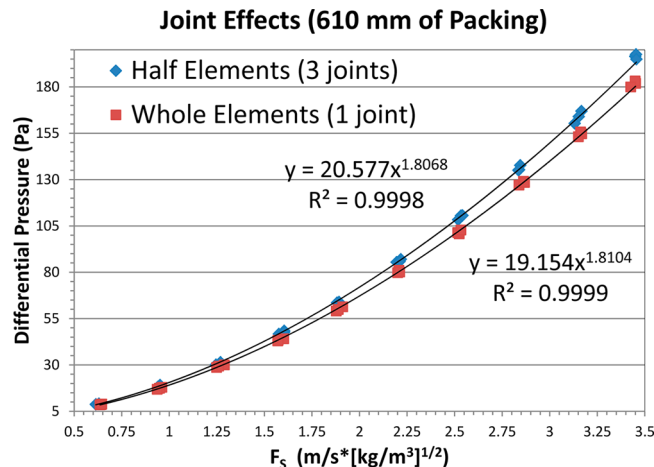


Figure 16. Effect of joints on pressure loss in 610-mm-tall packing stacks.

mixing or fluid stagnation, which is counterproductive to mass transfer.

CONCLUSIONS

Geometry Generation. CT scanning was shown to be a powerful and expeditious alternative to the traditional computer-aided drafting (CAD) method of geometry generation. The use of CT scans permitted generation of the base geometry in just over 7 h. This time could be reduced to mere minutes if a cone beam and area detector were employed for the scan. Scan-based geometry generation exceeds CAD in its ability to quantify resolution. The CT-based geometry provides fidelity equal to the minimum resolution of the scanner used. This is in sharp contrast to CAD, which relies on assumptions as to "relevant features" of the geometry or on the ability of the technician to accurately represent fine or complicated details. Therefore, CT-based geometry generation is preferable to CAD for complicated and irregular geometries.

Meshing. The convoluted and overlapping nature of structured packing represents a hurdle to the application of CFD simulations.

The goal of the CT scan is only to obtain an accurate representation of the packing. In so doing, a significant amount of extra data is obtained. The volume of data and the nature of the information present a barrier to efficient and accurate simulations. The surface wrapper was used to create useful surface information that could then be analyzed by CFD meshing and simulation software. The use of adaptive surface and volume meshing resulted in extremely high-quality mesh files for a variety of mesh growth rates and densities. The meshing algorithm employed here was very efficient; always requiring less than 30 h to generate highly refined surface and tetrahedral meshes and then convert them to the polyhedral equivalent. The prodigious meshes did require a large amount of physical memory (between 128 and 256 GB) for generation and conversion.

Adaptive meshing is extremely well suited to and beneficial in the simulation of structured packing. The complexity of packing geometry almost precludes the manual generation of a high-quality volume mesh. However, the decreased turn-around time required with adaptive meshing permits a more exhaustive study of various mesh parameters than can be achieved through manually specifying and improving a mesh. The ability to customize iterative mesh-improvement algorithms takes full advantage of unattended high-performance computing runs and results in dramatically improved mesh quality without requiring constant interaction by the researcher.

The use of polyhedral meshing resulted in mesh files with 80% fewer cells than a comparable tetrahedral volume mesh. This, in turn, yielded mesh files between 18 and 27 GB in size, as opposed to the expected tetrahedral mesh size of >300 GB. The polyhedral meshes displayed exceedingly high mesh quality as judged by both volume change and face quality metrics. Polyhedral meshing is ideal for the study of structured packing because of the combination of reduced file size when studying expansive geometries and their ability to conform to packing surfaces without reducing mesh quality or computational stability.

Simulation. Simulation with a $k-\epsilon$ turbulence model is capable of predicting nitrogen dry pressure loss with less than 10% error throughout the range of common distillation vapor rates through 250Y-series packings. CFD simulations provide a wealth of data not readily accessible by traditional experimental methods. The computation and display of streamlines enables researchers to quickly determine the regions of packing that exhibit poor flow performance. The use of contour plots enables an analysis of local variation in packing performance. Identifying the cause of such variation is critical to the improvement of distillation design, operation, and control.

These capabilities open the door to focused improvement of structured packing design. The unique data obtained from CFD simulations will enhance current understanding of distillation flow physics and provide a powerful diagnostic tool. Identifying specific causes of performance deficiencies will eliminate the need for extensive and expensive prototyping. Instead, potential improvements can be implemented to the CFD geometry and the resulting effects evaluated through flow simulations. This procedure will increase the gains made in each new model design and decrease the cycle time required to bring new designs to market.

A scaling analysis found 448 processors to be the most efficient use of resources to simulate a polyhedral mesh with 57 million volume elements. The use of more than 448 processors resulted in decreased computational speed relative to the increase in processor usage. The performance with 160 and 320 processors was also found to be relatively efficient although not equal to the optimum at 448 processors.

The $k-\epsilon$ turbulence model outperformed both the RSM and an analogous $k-\omega$ model when computing a constant-density, coupled-flow, and coupled-energy simulation with gravity effects. The $k-\omega$ model predicted a pressure loss more than 4% lower than the $k-\epsilon$ model. The RSM did not converge when run with the same simulation settings. Running the RSM simulation without the gravitational force and energy equation was also unstable. This sensitivity and long computation times make the RSM ill-suited for extensive use in modeling structured packing. Moreover, the high accuracy and available customization of the two-equation models largely negates the need for, and any potential benefit from, more complicated models.

Modeling. The two-layer realizable $k-\epsilon$ turbulence model predicted pressure losses 3.7–10.3% lower than experimental measurements for flow rates ranging from 0.61 to 3.66 (m/s) (kg/m^3) $^{1/2}$. This flow range is representative of the F factors commonly employed in industrial distillation columns. Therefore, the turbulence model used is capable of simulating single-phase flow across the range of distillation vapor rates to within 10% error.

Pressure loss was calculated using the Stichlmair model to compare simulation accuracy against a model commonly used in industry. Several different calculations were employed using both default packing specific parameters and those calculated specifically for the experimental and simulation geometry. The simulation outperformed all adaptations of the Stichlmair model in both accuracy and the nature of the response to increasing flow rate. This clearly demonstrates the power of CFD simulations. Even with a nearly 13-mm discrepancy in column diameter, the CFD simulations outperformed what is considered to be a robust model for predicting pressure loss. Moreover, CFD simulations not only predict performance, but also allow the researcher to assess the limiting factors that contribute to decreased performance.

Diagnostics. The extents of the velocity distribution were analyzed as an example of such an assessment. Negative flow was present along the entire length of the packing. Additional flow disruptions were observed at both the wiper band and the packing joints. The wiper bands induced a jump in the maximum velocity corresponding to the decrease in cross-sectional area. The packing joints caused a notable increase in negative flow rate. This corresponds to previous work that observed multiple flow disruptions at the packing joint.²⁸ This negative flow would result in back-mixing and increased pressure dissipation. For these reasons, it is apparent that the joint region introduces phenomena that act at cross purposes to efficient mass transfer.

A similar analysis conducted with area-weighted-average pressure proved similarly enlightening. Pressure loss was essentially linear with respect to progression through the structured packing. This relationship did not hold true at the packing joint. The joint imposed additional pressure loss similar in nature to that observed in flow through an orifice. In this way, each joint imposes a finite loss that accumulates through the column.

This effect was confirmed empirically by measuring the pressure loss through equivalent heights of half and whole packing elements. The greater number of joints in the half-element packing resulted in a greater overall pressure drop at all studied flow rates. From this result, it can be concluded that the requisite reboiler pressure is proportional to the number of joints installed in a column.

■ AUTHOR INFORMATION

Corresponding Author

*E-mail: rbeldr@che.utexas.edu.

Notes

The authors declare no competing financial interest.

ACKNOWLEDGMENTS

The authors of this work recognize the assistance of several organizations that, to a large degree, enabled this research. Sulzer Chemtech (<http://www.sulzerchemtech.com/>) provided the packings studied and expertise in their use. The Texas Advanced Computing Center (TACC, <http://www.tacc.utexas.edu>) at The University of Texas at Austin provided HPC and visualization resources and assistance in the utilization of those resources. CD-Adapco (<http://www.cd-adapco.com/>) provided their Star-CD software and licenses, along with troubleshooting in model development and convergence. The Jackson School of Geosciences (<http://www.jsg.utexas.edu/>) performed the CT scanning that resulted in the generation of the studied geometry. Dr. Roger Bonnecaze provided invaluable insight into fluid flow and advice on the interpretation of the data presented herein.

REFERENCES

- (1) *Distillation Column Modeling Tools*; Office of Industrial Technologies, Energy Efficiency and Renewable Energy, U.S. Department of Energy: Washington, D.C., 2001; p 1.
- (2) Doherty, M. F.; Fidkowski, Z. T.; Malone, M. F.; Raylor, R. Distillation. In *Perry's Chemical Engineers' Handbook*; Green, D. W., Perry, R. H., Eds.; McGraw-Hill: New York, 2008.
- (3) Seader, J. D.; Henley, E. J. *Separation Process Principles*, 2nd ed.; John Wiley & Sons: New York, 2006; p 756.
- (4) Tsai, R. E. Mass Transfer Area of Structured Packing. B.S. Thesis, The University of Texas, Austin, TX, 2010.
- (5) Petre, C. F.; Larachi, F.; Iliuta, I.; Grandjean, B. P. A. Pressure drop through structured packings: Breakdown into the contributing mechanisms by CFD modeling. *Chem. Eng. Sci.* **2003**, *58* (1), 163–177.
- (6) Larachi, F. V.; Petre, C. F.; Iliuta, I.; Grandjean, B. Tailoring the pressure drop of structured packings through CFD simulations. *Chem. Eng. Process.* **2003**, *42* (7), 535–541.
- (7) Ataki, A.; Bart, H. J. Experimental and CFD Simulation Study for the Wetting of a Structured Packing Element with Liquids. *Chem. Eng. Technol.* **2006**, *29* (3), 336–347.
- (8) Raynal, L.; Boyer, C.; Ballaguet, J. P. Liquid holdup and pressure drop determination in structured packing with CFD simulations. *Can. J. Chem. Eng.* **2004**, *82* (5), 871–879.
- (9) Szulczecka, B.; Zbicinski, I.; Gorak, A. Liquid flow on structured packing: CFD simulation and experimental study. *Chem. Eng. Technol.* **2003**, *26* (5), 580–584.
- (10) Raynal, L.; Royon-Lebeaud, A. A multi-scale approach for CFD calculations of gas–liquid flow within large size column equipped with structured packing. *Chem. Eng. Sci.* **2007**, *62* (24), 7196–7204.
- (11) Brunazzi, E.; Paglanti, A. Mechanistic pressure drop model for columns containing structured packings. *AIChE J.* **1997**, *43* (2), 317–327.
- (12) Meier, W.; Hunkeler, R.; Stocker, W. D. Sulzer Mellapack-Eine neue Geordnete Packing fur Stoffaustausch-Apparate. *Chem. Ing. Tech.* **1979**, *51*, 119.
- (13) Olujic, Z. Effect of column diameter on pressure drop of a corrugated sheet structured packing. *Trans. Inst. Chem. Eng.* **1999**, *77*, 505.
- (14) Rocha, J. A.; Bravo, J. L.; Fair, J. R. Distillation columns containing structured packings: A comprehensive model for their performance. 1. Hydraulic models. *Ind. Eng. Chem. Res.* **1993**, *32*, 641.
- (15) Rocha, J. A.; Bravo, J. L.; Fair, J. R. Distillation columns containing structured packings: A comprehensive model for their performance. 2. Mass transfer model. *Ind. Eng. Chem. Res.* **1996**, *35*, 1660.
- (16) Mahr, B.; Mewes, D. CFD Modelling and Calculation of Dynamic Two-Phase Flow in Columns Equipped with Structured Packing. *Chem. Eng. Res. Des.* **2007**, *85* (8), 1112–1122.
- (17) Mahr, B.; Mewes, D. Two-phase flow in structured packings: Modeling and calculation on a macroscopic scale. *AIChE J.* **2008**, *54* (3), 614–626.
- (18) Jafari, A.; Zamankhan, P.; Mousavi, S. M.; Pietarinen, K. Modeling and CFD simulation of flow behavior and dispersivity through randomly packed bed reactors. *Chem. Eng. J.* **2008**, *144*, 476–482.
- (19) Bai, H.; Theuerkauf, J.; Gillis, P. A.; Coupled, A. DEM and CFD Simulation of Flow Field and Pressure Drop in Fixed Bed Reactor with Randomly Packed Catalyst Particles. *Ind. Eng. Chem. Res.* **2009**, *48*, 4060–74.
- (20) Fernandes, J.; Simoes, P. C.; Mota, J. P. B.; Saatdjian, E. Application of CFD in the study of supercritical fluid extraction with structured packing: Dry pressure drop. *J. Supercrit. Fluids* **2008**, *47* (1), 17–24.
- (21) Fernandes, J.; Lisboa, P. F.; Simoes, P. C.; Mota, J. P. B.; Saatdjian, E. Application of CFD in the study of supercritical fluid extraction with structured packing: Wet pressure drop calculations. *J. Supercrit. Fluids* **2009**, *50*, 61–68.
- (22) Ketcham, R. A. New Algorithms for Ring Artifact Removal. In *Developments in X-Ray Tomography V*; Bonse, U., Ed.; SPIE Press: Bellingham, WA, 2006; p 63180O.
- (23) Green, C. W. Hydraulic Characterization of Structured Packing via X-Ray Computed Tomography. Ph.D. Thesis, The University of Texas, Austin, TX, 2006.
- (24) STAR-CCM+ User Manual; CD-Adapco: Melville, NY.
- (25) Thompson, J. F.; Bharat, S.; Weatherill, N. P. *Handbook of Grid Generation*, 1st ed.; CRC Press: Boca Raton, FL, 1998; p 1200.
- (26) Durran, D. *Numerical Methods for Wave Equations in Geophysical Fluid Dynamics*, 1st ed.; Springer-Verlag: Berlin, Germany, 1999; p 465.
- (27) Stichlmair, J.; Bravo, J. L.; Fair, J. R. General model for prediction of pressure drop and capacity of countercurrent gas/liquid packed columns. *Gas Sep. Purif.* **1989**, *3* (1), 19–28.
- (28) Owens, S. A.; Kossmann, A.; Farone, J.; Eldridge, R. B.; Ketcham, R. A. Flow Field Visualization in Structured Packing Using Real Time X-ray Radiography. *Ind. Eng. Chem. Res.* **2009**, *48* (7), 3606–3618.
- (29) Green, C. W.; Farone, J.; Briley, J. K.; Eldridge, R. B.; Ketcham, R. A.; Nightingale, B. Novel Application of X-ray Computed Tomography: Determination of Gas/Liquid Contact Area and Liquid Holdup in Structured Packing. *Ind. Eng. Chem. Res.* **2007**, *46* (17), 5734–5753.